OptoRheo: Simultaneous *in situ* micro-mechanical sensing and 3D imaging of live cell cultures.

Authors: Tania Mendonca[1], Katarzyna Lis-Slimak[2], Andrew B. Matheson[3], Matthew G. Smith[4], Akosua B. Anane-Adjei[5], Robert Cavanagh[5], Lynn Paterson[3], Paul A. Dalgarno[3], Cameron Alexander[5], Manlio Tassieri[4], Catherine L. R. Merry[2] and Amanda J. Wright[1]

[1] Optics and Photonics Research Group, Faculty of Engineering, University of Nottingham, Nottingham, NG7 2RD, UK

[2] Stem Cell Glycobiology Group, Nottingham Biodiscovery Institute, School of Medicine, University of Nottingham, Nottingham, NG7 2RD, UK

[3] Institute of Biological Chemistry, Biophysics and Bioengineering, School of Engineering and Physical Sciences, Heriot Watt University, Edinburgh, EH14 4AS, UK

[4] Division of Biomedical Engineering, James Watt School of Engineering, University of Glasgow, Glasgow, G12 8LT, UK

[5] School of Pharmacy, University of Nottingham, Nottingham NG7 2RD, UK

Abstract

Biomechanical cues from the extracellular matrix (ECM) are essential for directing many cellular processes, from normal development and repair to disease progression. To better understand cell-matrix interactions, we have developed an optical instrument combining light sheet fluorescence microscopy with particle tracking microrheology. We name this new instrument OptoRheo. OptoRheo lets us image cells in 3D as they proliferate over several days while simultaneously sensing the biomechanical properties of the surrounding extracellular and pericellular matrix at a sub-cellular scale. OptoRheo can be used in two operational modalities to extend the dynamic range of microrheology measurements, making the instrument suitable for different cell culture systems. We corroborated this by

characterising the ECM surrounding live breast cancer cells in two distinct culture systems, 3D hydrogels and suspension culture. This cutting-edge instrument will transform the exploration of drug transport through complex cell culture matrices and optimise the design of the next-generation disease models.

Introduction

Cells sense and respond to the mechanical properties of the extracellular matrix (ECM) at a cellular length scale, using traction forces to probe stiffness [1], steer migration [2,3] and influence cell fate [4]. Simultaneously, the ECM is continuously remodelled by cells as they exert these traction forces [5] during cell migration and morphological re-arrangement [6]. Anomalies in the mechanical properties of the ECM play significant roles in the development of pathologies such as cancer [7] and fibrosis [8], often establishing barriers to therapeutic intervention [9]. Modelling and understanding the cellular influence on ECM biomechanics are challenging processes given the wide range of mechanical environments experienced in health and disease. In healthy tissues, the elastic modulus has been reported to range from tens of Pa (e.g., brain, lung) to well above 10 KPa (e.g., skeletal muscle, bone), with disease states such as cancer and fibrosis showing a significant change in stiffness (e.g., from 800 Pa for normal breast to more than 4KPa in breast cancer) [10]. Moreover, the full mechanical characterisation of the ECM also contains a viscous component that may influence cell behaviour, although this property is often disregarded in the literature. The recent development of engineered hydrogels with tuneable mechanical properties [11,12] have made it possible to recreate elements of the ECM micro-architecture *in vitro* and reveal the influence of ECM viscoelasticity on cell processes [13,14]. Despite these advances and their importance, the mechanistic processes of cell-matrix interactions remain poorly understood. For instance, do cells ‘prime’ their local environment prior to migrating or do they exploit existing weaknesses in the ECM and migrate accordingly? These unanswered questions call for

minimally invasive optical approaches to monitor changes in the microscopic mechanical properties of the ECM, *in situ* and in real time, local to proliferating cells over many days.

To address this aim, OptoRheo combines three different microscopy techniques into a single instrument, enabling live fluorescence imaging deep in 3D cell cultures and microrheology measurements of the ECM within the same region of interest, local to and far from the cells. 3D fluorescence imaging is achieved using a new version of reflected light sheet fluorescence microscopy (LSFM) [15–18] built on a commercial inverted microscope body to image hundreds of microns deep from the coverslip, within live 3D cell cultures and with sub-cellular resolution. The sample is kept completely stationary during z-scanning, with no perturbation or contamination risk from dipping lenses, both crucial for ensuring that observation does not influence the mechanical or biological properties of the sample. This novel configuration allows for delicate samples such as hydrogel scaffolds to be imaged simply in off-the-shelf chambered coverslips. To extract the viscoelastic properties of the ECM non-invasively, OptoRheo tracks the thermally driven Brownian motion of micro-scale probes across a wide frequency range. The inert probes can be embedded in the hydrogel during encapsulation [6,19–21] or even internalised into cells [22] to probe intra-cellular viscoelasticity. In suspension cultures, an optical trap can be used to hold the probe in the field of view within the cells' microniche during the measurement time-window [23]. This approach makes the instrument suitable for micro-mechanical sensing in a wide range of cell culture substrates such as those commonly employed in the biomedical field. Finally, OptoRheo incorporates optional multiplane imaging that can be used to extend microrheology to 3D in a configuration similar to the one developed for OptiMuM [24], to achieve a full 3D characterisation of the extracellular microenvironment.

To highlight the capability of OptoRheo, we present data obtained from the analysis of two systems seeded with human-derived MCF-7 breast cancer cells, either (I) encapsulated as clusters in 3D hydrogels or (II) as spheroids maintained in suspension culture. In the case of

hydrogel scaffolds, matrix stiffness was measured using passive particle tracking microrheology without the use of an optical trap or multiplane imaging, whereas in the case of suspension cultures, the optical trap was implemented along with multiplane imaging. Imaging and microrheology were performed sequentially at multiple regions within the samples at depths of 150 µm - 400 µm from the coverslip. In the case of the hydrogels, the samples were monitored over three days to reveal microscale variations in the elastic properties of the ECM near to and away from cells. When studying spheroids in suspension the optical trap was used to place and hold the probes in user-defined locations and extract the relative viscosity of the media near the spheroids. Notably, in both the cases our measurements were found to be sensitive to local spatio-temporal variations in the biomechanical properties of the culture medium. As we aim to show, our multimodal and minimally invasive approach opens a wide range of future opportunities for physiologically relevant, long-time course investigations of cell-ECM interactions in fragile live cell culture samples. We anticipate that this approach will be applied to increasingly complex and relevant *in vitro* models, providing an essential insight into the previously opaque mechanistic control of cell behaviour by the ECM in health and disease.

Results

3D imaging deep in live cell cultures

A schematic representation of OptoRheo can be seen in Figure 1. 3D light sheet fluorescence microscopy (LSFM) is achieved by projecting a thin, planar excitation beam limited to the detection plane of the microscope and collecting the emitted fluorescence at a 90° angle to the illumination plane [25,26]. For deep imaging of live 3D cell cultures, the light sheet illumination was introduced using a 10 mm 90:10 (Reflectance: Transmittance) beam splitter cube placed in the sample chamber prior to casting the gel

alongside it (Figs 1, 2 and S1). This LSFM approach has multiple advantages; deep and fast fluorescence imaging with low phototoxicity [27] and minimal sample perturbation during imaging, while being cost-effective and modular. The glass beam splitter cube can be sterilized for reuse and placed either inside or outside the sample chamber to provide flexibility to adapt to different experimental conditions.

Unlike some other prism or mirror based LSFM solutions [15,28,29], 3D image generation was achieved here by scanning the light sheet and not the sample. Notably, this allows the sample to be kept stationary and undisturbed throughout data collection, which is essential for imaging delicate samples prepared in soft hydrogels (Fig 2A) or liquid suspension media over multiple days. The light sheet itself was generated using a cylindrical lens, the properties of which set the thickness of the light sheet and influences the axial resolution and optical sectioning capabilities of the microscope. In the presented configuration, the measured axial resolution of the detection optics of the LSFM on OptoRheo was 1.09 µm for λ_{ex}\ λ_{em} = 532 nm \ 580 nm which agrees closely with theory (1.1 µm) (Fig 2B).
A scanning galvanometer mirror was placed conjugate to the cylindrical lens using a 4f system, so that tilting the galvanometer mirror translated to a Z-shift in position of the light sheet at the sample (Fig 1). Acquiring Z-stacks involved synchronisation of the galvanometer mirror with a piezoelectric objective scanner that moved the objective lens, ensuring that the illumination and imaging planes remained co-aligned and synchronised throughout the scan. The light sheet remained at optimal thickness (~3 µm for all three colour channels, see Methods) over a field of view of ~100 µm. However, image tiling could be achieved within a region 4-6 mm from the beam splitter cube to increase the field of view. This required shifting the light sheet focus laterally by moving the position of the cylindrical lens. The shifted position of the beam splitter was compensated by tilting the galvanometer mirror to image the new focal position.

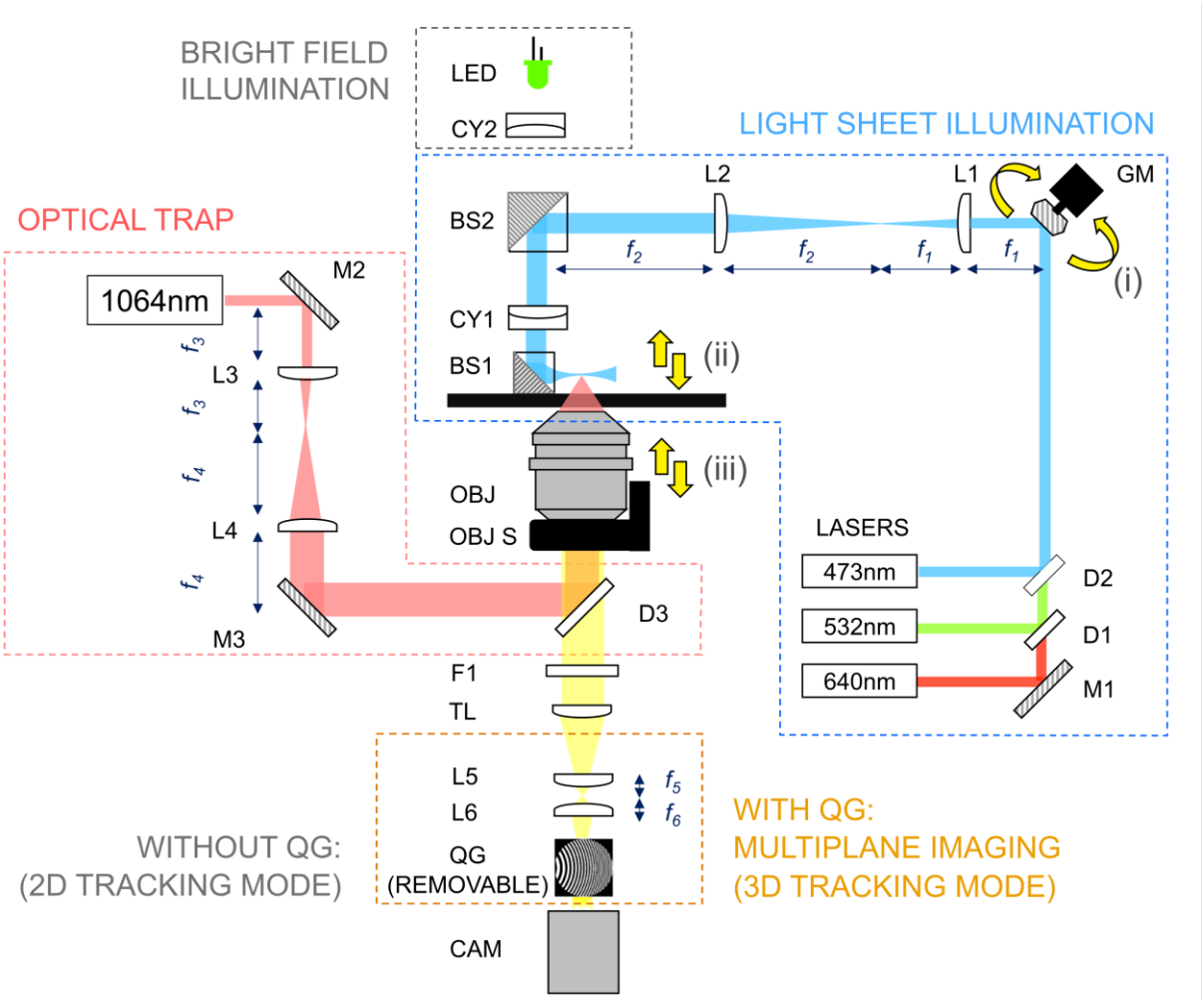

137

138 Figure 1: **A schematic representation of the OptoRheo instrument**. Components: Lasers
139 – 473 nm, 532 nm and 640 nm lasers provide the light sheet illumination while a 1064 nm
140 laser is used for optical trapping. M1- M3 – mirrors; D1-D3 – dichroic mirrors; L1-L6 –
141 achromatic doublets, L1 and L2 form a 8.3 x beam expander and are part of a 4f system with
142 the galvanometer mirror (GM) and a beam splitter (BS2); CY1, CY2 – cylindrical lenses;
143 BS1, BS2 – beam splitter cubes; OBJ – objective lens; OBJ S – piezoelectric objective
144 scanner; F1– fluorescence emission filter; TL – tube lens, QG – quadratic gratings and CAM
145 – camera. Yellow arrows indicate synchronised motion of (i) the galvanometer mirror, (ii) the
146 projected light sheet and (iii) the objective lens (using a piezoelectric objective scanner). The
147 quadratic gratings slide in and out of the optical path to enable 2D and 3D particle tracking.
148 The quadratic gratings are removed for the LSFM imaging.

149

OptoRheo is fitted with a stage-top incubator that regulates temperature, CO_2 and humidity around the sample, allowing long time-course experiments. The current configuration of OptoRheo uses a 60x objective lens with a 1.5 mm working distance and a numerical aperture (NA) of 1.1, selected to image deep into a sample, but with a high enough NA for optical trapping. For the data presented in this work, z-scans were typically recorded 150 µm - 400 µm from the coverslip (Fig 2C). The multiplane grating breaks up the field of view into nine planes to enable 3D tracking [24] and therefore, is not required for LSFM imaging and can be easily removed by means of a slider. Additionally, the quadratic gratings used were optimised for a particular wavelength (543 nm) making them unsuitable for multicolour imaging.

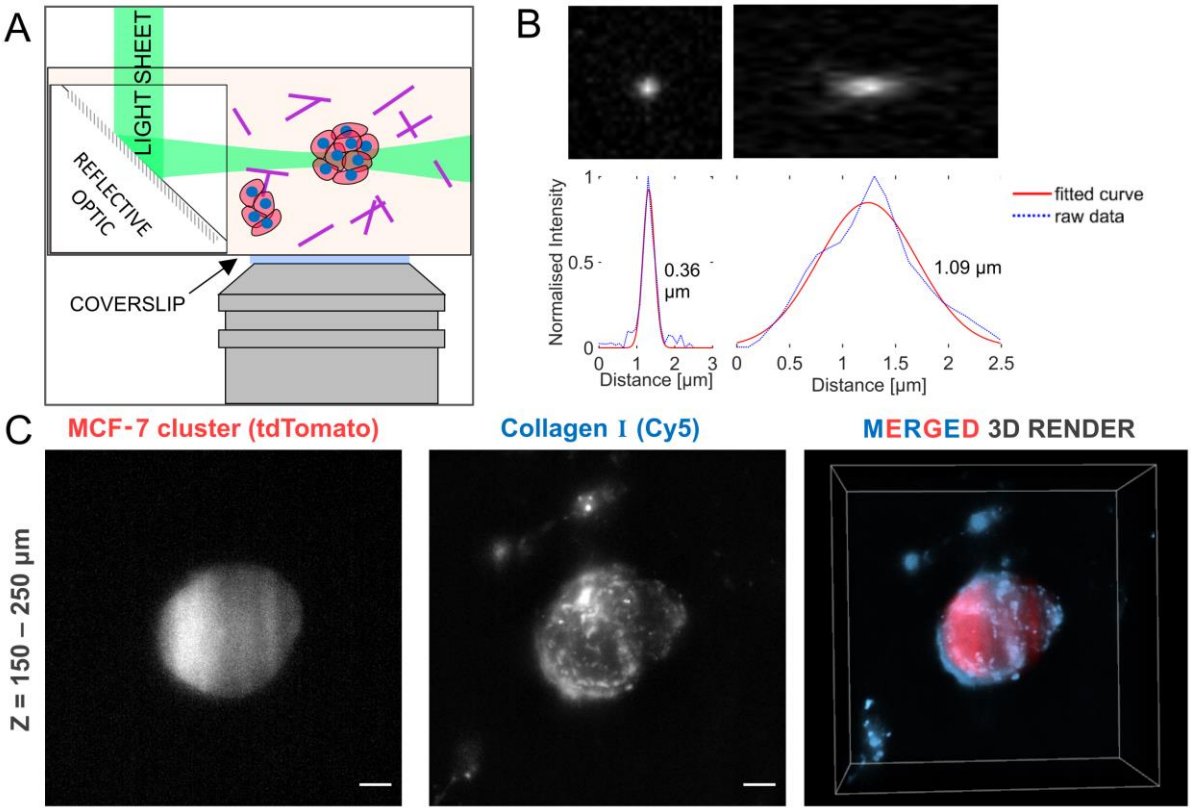

Figure 2: **Light sheet fluorescence microscopy (LSFM) with OptoRheo.** A. Light sheet generation at the sample is enabled by a beam splitter cube placed within the sample

chamber. Sample consists of cell clusters (represented by red circles with blue centres) and collagen (purple lines). B. Lateral (left) and axial (right) point spread functions (PSFs) of the system along the XY (0.36 µm FWHM) and YZ (1.09 µm FWHM) planes measured using fluorescent sub-diffraction sized microspheres (diameter = 200 nm, λ_{ex} / λ_{em} = 532 nm / 580 nm) at ~200 µm from the coverslip. C. From left to right, maximum intensity projection (z = 150 – 250 µm from the coverslip) of a volume showing a cluster of tdTomato (λ_{ex} / λ_{em} = 554/ 581 nm) MCF-7 cells, the same volume showing Cy5 (λ_{ex} / λ_{em} = 649/ 666 nm) labelled collagen I and a 3D rendering of the merged channels. Scale bars = 5 µm.

Microrheology of gels and suspension cultures

The viscoelastic properties of biomaterials can be extracted non-invasively using particle tracking microrheology as developed by this group and others [23,24,30]. This involves a statistical analysis of the residual Brownian motion of micron-sized spherical probes, whose temporal behaviour can be described by means of a Generalised Langevin equation [30]. For this purpose, polystyrene microsphere probes were seeded in the cell culture samples under sterile conditions (Fig 3A). For hydrogel-based cell culture systems, the diameter of the microsphere probes (6 µm) was selected so that the Brownian motion of the probes were constrained by the hydrogel polymer network. A small field of view (typically 14 µm x 14 µm) was recorded around the microsphere probe (Fig 3B) to track the trajectory of each probe (Fig 3C) at a relatively high frame rate (~ 300 Hz) for broadband microrheology. This was done while switching the illumination to transmission mode using a LED source to avoid introducing fluorescence bleaching-related errors in particle tracking (Fig 1). A second cylindrical lens (CY2 in Fig 1) was placed in the LED light path to compensate for the presence of the light sheet forming cylindrical lens (CY1 in Fig 1) and produce uniform illumination. An analysis of the mean squared displacement (MSD) of the confined

191 microspheres (Fig 3D) gives the elastic (G') and viscous (G'') moduli of the surrounding gel
192 (Fig 3E).
193
194

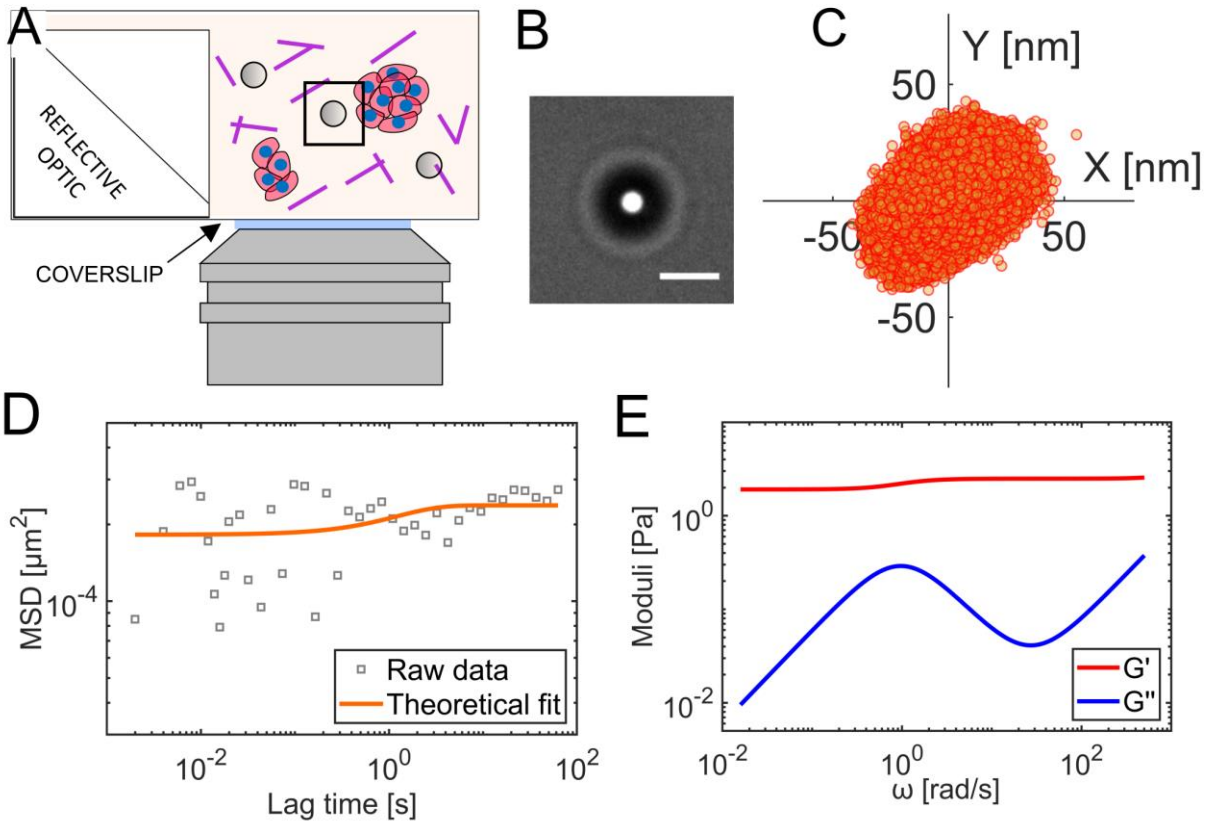

195

196 Figure 3: **Passive microrheology without optical trapping.** A. Microsphere probes were
197 seeded in hydrogel for performing passive microrheology. B. Measurements involve imaging
198 small regions of interest (typically 14 μm x 14 μm as shown) around individual probes (6 μm
199 diameter) at a high frame rate. Scale bar: 4 μm C. Particle positions (orange circles) in a 2D
200 plane. D. The mean squared displacement (MSD) provides a measure of gels' compliance,
201 here modelled by using a simple expression: $MSD(t) = A + B\left(1 - \exp\left(-\frac{t}{\tau}\right)\right)$, where A, B
202 and τ are fitting parameters. The model helps to minimise the detrimental effect of
203 experimental noise, especially at short time scales. E. The elastic (G') and viscous (G'')
204 moduli of the gel over a range of frequencies can be evaluated from the analysis of the MSD
205 fits.

In liquid media and suspension cultures, microsphere probes sediment to the coverslip over time with a rate dependent on the gravitational force, the buoyancy of the microsphere and the viscosity of the medium [31]. In aqueous liquids, this sedimentation rate is about 20 µm/s for microspheres with a 3 µm radius, thus preventing long-term (i.e. tens of minutes) tracking of the probe trajectory, which are needed for microrheology calculations. Therefore, when working with liquids we used an optical trap (Fig 4A) to hold the probe in the field of view and at the required location relative to the cell/s of interest during the measurement time. The trapping force acting on the microsphere was kept very low ($<10^{-6}$ N/m) by controlling the laser power, to maximise the amplitude of the residual Brownian motion, increasing the sensitivity of the microrheology measurement and the frequency range. The confined Brownian motion of the microsphere could then be recorded at ~ 300 Hz in 3D by using the multiplane detection approach [24,32] by inserting a removable pair of quadratic gratings (QG) in the detection path before the sCMOS camera (Fig 1 and 4B). The quadratic grating pair focus light from nine object-planes as an array onto the camera sensor for instantaneous 3D imaging without the need of any mechanical moving parts [24,32] (Fig 4B). This method allows the tracking of the microsphere motion in all three dimensions simultaneously (Fig 4C), revealing spatial variation of the sample's viscoelastic properties. However, the smallest variance in particle position we could reliably measure with the present configuration was 30 nm in z, compared to 15 nm in xy 15 nm. Therefore, tracking in z was unreliable for our gel samples where the motion is typically less than 50nm (see Fig 3C).

We validated our microrheology measurements from the 3D particle tracking mode of OptoRheo by using water, a well characterised Newtonian fluid. We extended our previous work [24] by measuring the 3D trajectories of microsphere probes from 50 to 400 µm away from the coverslip, without the use of any aberration correction, thus enabling microrheology measurements at the same sample depths as our light-sheet imaging experiments. It is important to note that most studies employing optical trapping report measurements taken at

<100 µm from the coverslip [33]. The use of water immersion and a correction collar allowed us to achieve trap stiffness k values of k_x= 3.2 x 10^{-7} ± 0.3 x 10^{-7} N/m along the x axis, k_y = 3.2 x 10^{-7} ± 0.5 x 10^{-7} N/m along the y axis and k_z = 6.7 x 10^{-7} ± 1.2 x 10^{-7} N/m along the z axis (mean ± standard deviation) over this large range of distances from the coverslip. Relative viscosity (ratio of viscosity of an aqueous solution to the viscosity of water at the same temperature) could be evaluated in 3D by analysing the normalised position autocorrelation function (NPAF) for x, y and z at depths ranging from 50 µm to 400 µm from the coverslip. In particular, the relative viscosity can be read "*at a glance*" from the abscissa of the NPAF intercept e^{-1}, when the NPAF is plotted versus a dimensionless lag-time $\tau^* = k\tau/(6\pi a\eta_s)$; where k is the trap stiffness, τ is the lag-time (or time interval), a is the probe radius, and η_s is the Newtonian viscosity expected for the pure solvent [34] (Fig 4D). Figure 4E shows the mean x, y and z relative viscosity ± standard deviation, performed at different depths (see Methods). Over the range of recorded measurements, the measured mean relative viscosity (over x, y and z) remained stable with depth (i.e., 1 ± 0.05).

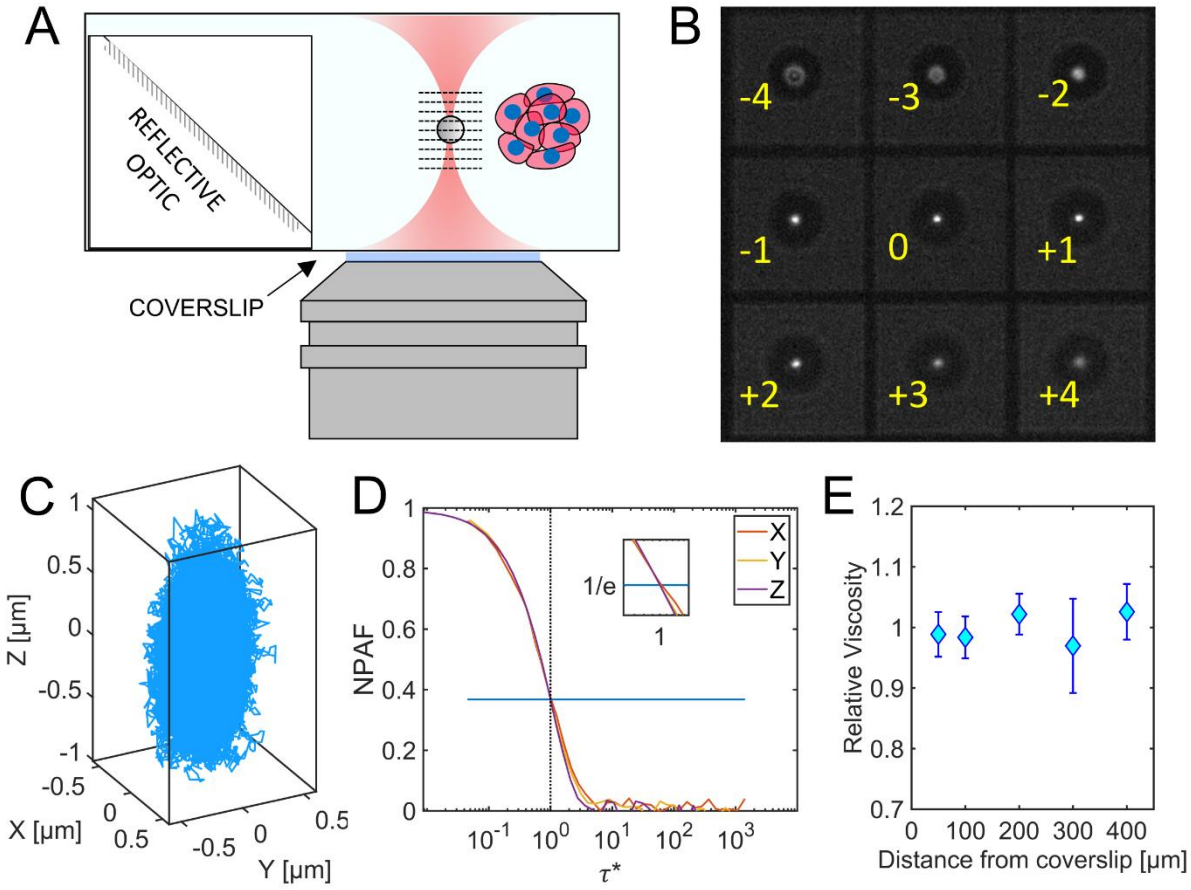

Figure 4: **Microrheology with an optical trap and multiplane detection** (3D particle tracking mode) in an aqueous solution. A. An optically trapped microsphere is imaged in 9 planes simultaneously (planes represented by dashed lines). B. Captured image of nine separate Z planes (Δz = 0.79 μm). The planes (labelled from number -4 to +4) are simultaneously recorded at the camera sensor to extract the 3D trajectory. C. The resulting 3D trajectory of optically trapped microsphere in water. D. The normalised position autocorrelation function (NPAF) versus a dimensionless time, τ^*. E. The mean ± standard deviation of the relative viscosity measured at each position over a range of depths.

Monitoring ECM stiffness in hydrogel-encapsulated 3D cell culture

In order to test the ability of OptoRheo to evaluate biomechanical properties of the ECM in real time, clusters of human-derived MCF-7 cancer cells expressing the tdTomato fluorescent protein were grown in a hydrogel-encapsulated cell culture matrix [11,35]. Changes in the ECM stiffness around these cells have been correlated with cancer progression and metastasis, and have been shown to alter drug resistance [36,37]. Complementary multi-colour 3D LSFM imaging allowed cells and labelled matrix components (i.e. collagen I) from the same locations to be captured in separate colour channels. These volume images could be overlaid and combined with microrheology measurements to map the changing biomechanical properties to the changing morphology of the sample at the microscale. This approach was used to compare four different complex systems made of hydrogels with and without (i) collagen and (ii) cells.

Environmental control on OptoRheo allowed samples to be kept under physiological conditions over three days, making it possible to select microsphere probes located near cell clusters and re-visit them multiple times over the duration of the experiment to follow the changing ECM properties experienced by the cells over time (Fig 5A and 5B). The results from these long-time course experiments highlight a dynamic microenvironment. Viscoelasticity measured at individual probes changed over time as cell clusters proliferated and changed their relative distance from the probes (Fig S2) which could be extracted from LSFM images. Our localised measurements reveal heterogeneities in viscoelasticity within all the hydrogel cell culture samples studied, including naked gels (Fig 5C, 5D and Supplementary Table S1). Heterogeneities were found to be greatest in the most complex system studied, that of gels seeded with collagen and cells. These gels showed a factor of 3 times greater variance in G' values than each of the other three gel compositions, which were comparable in variability (Fig 5C, 5D and Supplementary Table S1). The variation in G'' values of the gels with collagen and cells (n = 20) on the other hand was a factor of ~ 6.5 times more than in naked gels (n = 11) and a factor of ~ 12 times more in both gels seeded with collagen alone (n = 11) and gels with cells but without collagen (n = 19).

There was no clear trend in viscoelastic behaviour with increasing distances, suggesting more complex interactions may be taking place, potentially involving matrix components secreted into the gels by the encapsulated cells. However, there was greater change in both viscoelasticity and relative distance between the probes and cell clusters in gels supplemented with collagen as opposed to those without (Fig S2). Interestingly, we were able to detect a greater heterogeneity in both G' and G'' values in gels with collagen and cells than with either without cells (Fig 5C and 5D), demonstrating the importance of incorporating control conditions when interpreting changes in mechanical environments around encapsulated cells.

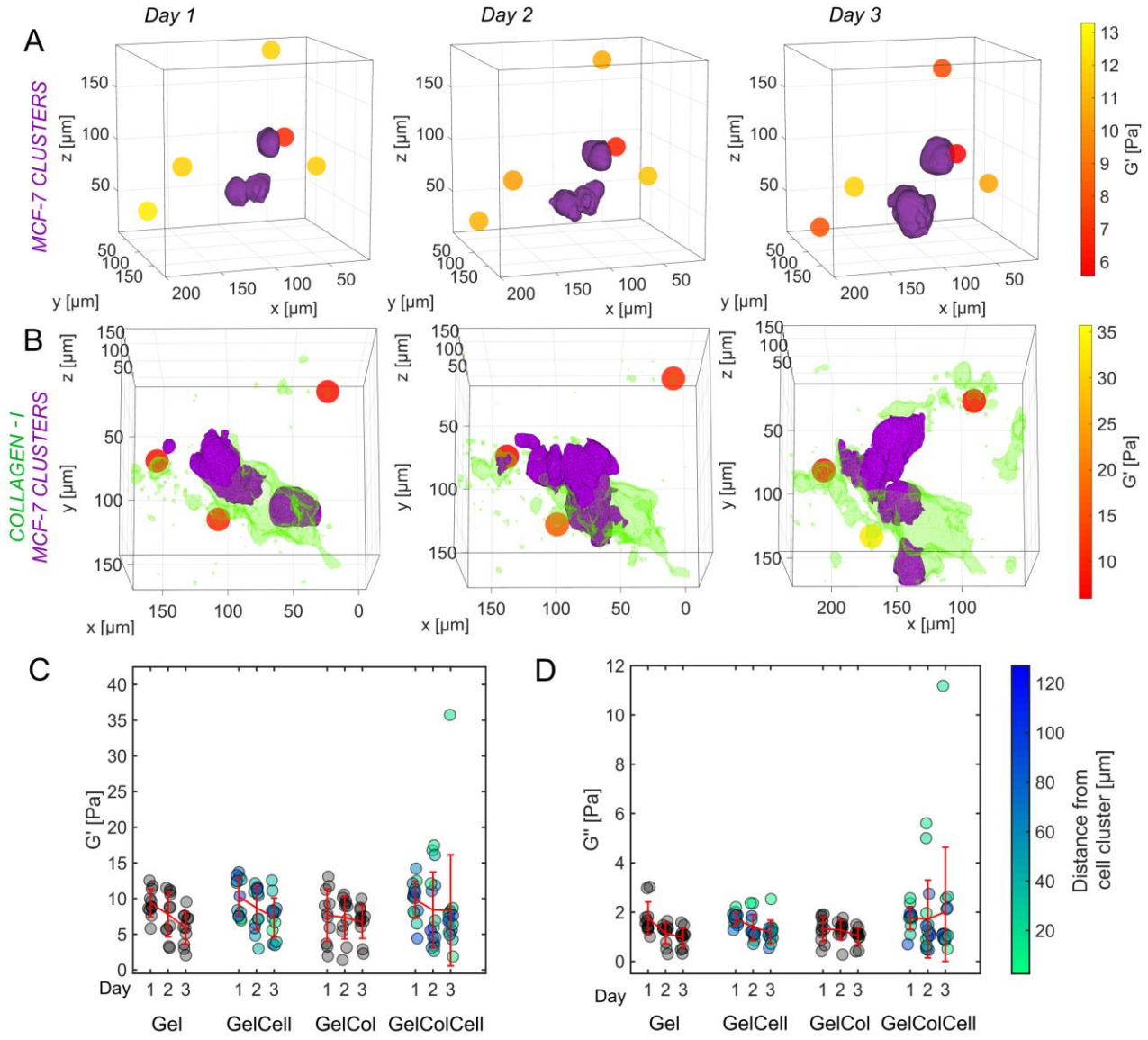

Figure 5: **Local stiffness measured in live 3D cell cultures with different compositions**. A. Example biomechanical maps produced by OptoRheo of MCF-7 clusters expressing tdTomato (shown in purple) encapsulated in hydrogels and B. MCF-7 clusters from the same cell line in hydrogel supplemented with collagen I labelled with Cy5 (shown in green) monitored over three days. Spheres depict microsphere probes (not to scale) assigned a colour to reflect the local stiffness measured in terms of the material's elastic modulus (G'). C. & D. The variation in the material's viscoelastic moduli (G' & G'') over three days for different matrix conditions where Gel stands for hydrogel only, GelCell is hydrogel and cells (including data from A), GelCol is hydrogel with collagen, and GelColCell stands for hydrogel

with cells and collagen (including data from B). The blue-green gradient denotes distance from the cell cluster. Black represents the samples with no cells.

Mapping relative viscosity local to spheroids in suspension culture

The second scenario tested as a proof-of-concept, was to acquire 3D images and microrheology measurements near spheroids in suspension culture. Spheroids were grown from the same MCF-7 cancer cell line as in the peptide hydrogel cultures and were used two days after seeding at a size of ~1 mm in diameter. As both 3D imaging and microrheology on OptoRheo do not involve moving the sample, these spheroids could be maintained in liquid media without the need to immobilise them in agarose or any other hydrogel matrix, unlike most conventional LSFM instruments. Volume images near the edges of spheroids, were acquired by tiling multiple overlapping imaging volumes of 200 µm x 200 µm x 200 µm (between 150 µm – 350 µm from the coverslip) (Fig 6A). Once the images were acquired, the instrument was switched from LSFM modality to 3D particle tracking mode by sliding the quadratic gratings into the optical path and with illumination in transmission (QG in Fig 1). The optical trap enabled microsphere probes to be individually trapped and positioned in 3D with the XY stage and the piezoelectric objective scanner to make measurements at selected locations near the edge of the spheroids (Fig 6A inset).

Our measurements show an apparent increase in relative viscosity with decreasing distance (4 µm, n = 4; 6 µm, n = 4; 12 µm, n = 3 and 30 µm, n = 7) between the centre of the microsphere and the surface of the spheroid (n = 2 spheroids) (Fig 6A, 6B and 6C). Viscosities could be extracted in 3D by resampling the recorded 3D trajectories along any desired axis, calculating the MSD, and then using Fick's Law (see methods). Such angle-by-angle analysis reveals higher relative viscosity values perpendicular to the surface of the spheroid as compared to parallel to the surface, with the anisotropy increasing as the probe

339 approaches the surface (Fig 6B). This trend is in agreement with predictions from Faxén's
340 law which describes the increased hydrodynamic drag experienced by objects near solid
341 surfaces and manifests itself in an increase in apparent viscosity, albeit our measured values
342 are lower than the predictions [38] (dashed black line in Fig 6C). The lower values could
343 potentially be attributed to the spheroid surface being irregular and not completely inelastic.
344 Additionally, the presence of salts in the nutrient medium may reduce electrostatic
345 interactions at surfaces as corroborated by control measurements at corresponding
346 distances from the inert glass coverslip in the same medium without the presence of the
347 spheroids (red line in Fig 6C).
348
349

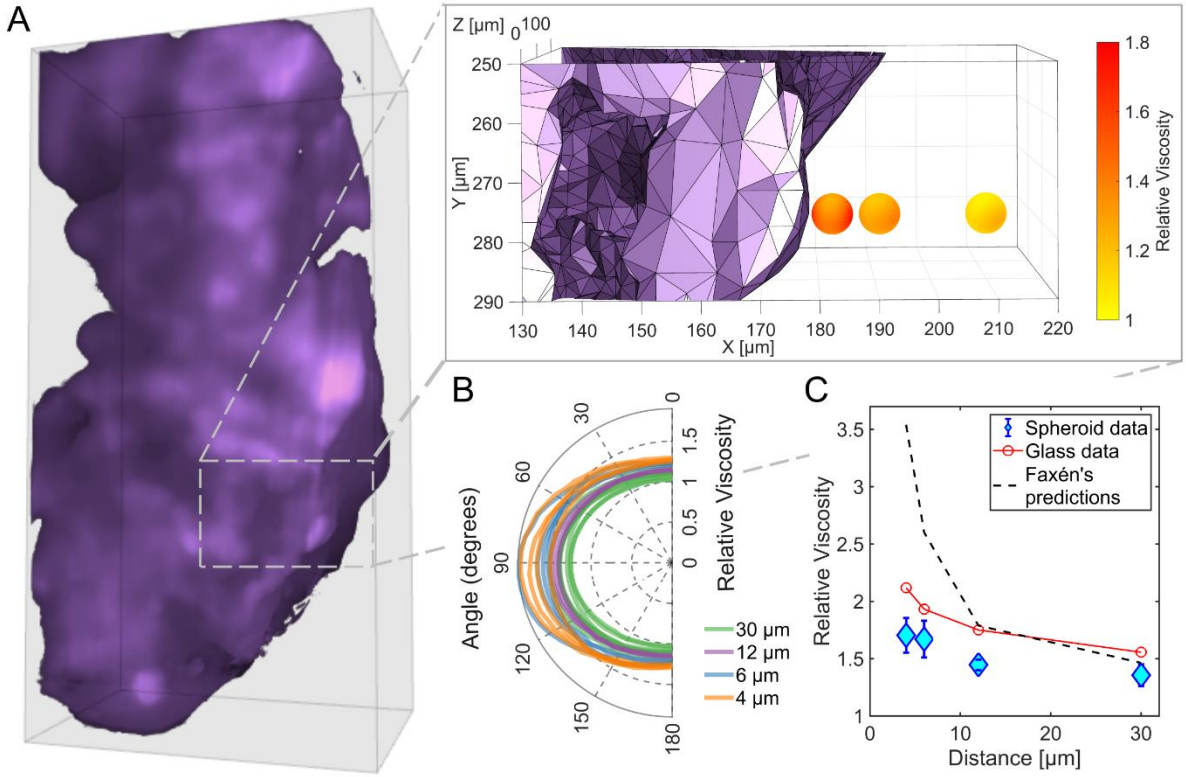

350
351 Figure 6: **Viscosity near spheroid**. A. 3D rendering of a section of a spheroid of MCF-7
352 cells expressing td-Tomato (relative dimensions: 200 µm x 400 µm x 100 µm (150-250 µm
353 from the coverslip)). The inset shows one of the areas where viscosity (relative to the
354 solvent) measurements were acquired at incremental distances from the spheroid surface –

three measurements (4 µm, 12 µm and 30 µm from the spheroid surface) are depicted as spheres (not to scale). The colour gradient for each sphere represents the relative viscosity sampled by angle at each measurement position. A fourth position (6 µm) has not been shown to aid visualisation. B. Relative viscosity measurements in a plane perpendicular to the spheroid surface, passing through the highest and lowest measured viscosity at the probe position. C. Mean ± standard deviation of relative viscosity measurements of the nutrient media at each position for a direction perpendicular to the spheroid surface (blue) and glass (red), showing increased apparent viscosity at positions closer to the surface but lower than values predicted from Faxén's law (black dashed line).

Discussion

To understand how cells interact with and remodel their surrounding matrix, it is crucial to not only visualise cell clusters in 3D, but also to map these images to the micro-mechanical properties of the matrix local to, and distant from the cells. In this study, we have introduced an integrated instrument, OptoRheo, that combines light sheet fluorescence microscopy (LSFM) with non-invasive microrheology to enable a more complete understanding of cell-matrix interactions. The new LSFM configuration presented here is straightforward to implement and does not require the use of bespoke, expensive optics. This reflected configuration allows for samples to be prepared and mounted as on any commercial inverted microscope, using off-the-self sample chambers and a stage-top incubator to control temperature, humidity and CO_2 throughout experiments, enabling delicate hydrogel-based cell culture samples to be studied over multiple days. With the ability to optically trap microrheological probes when required, we have demonstrated the capability of the instrument to study aqueous (suspension culture) as well as soft solid (hydrogel) environments. This modular functionality with a gratings-based approach allows OptoRheo to transition from 2D to 3D particle tracking effortlessly. We provide experimental evidence of this approach by following changes in matrix viscoelasticity in 2D in hydrogel-encapsulated

382 cell cultures over three days and viscosity in 3D near spheroids. Our localised rheological
383 measurements reveal extensive heterogeneities at the microscale in hydrogel-encapsulated
384 cell cultures. These heterogeneities are seen both in matrix stiffness and in the distribution of
385 matrix components, with fluorescently tagged collagen aggregating in defined regions,
386 particularly in the pericellular space (Fig 5B). Furthermore, we demonstrate 3D imaging of
387 spheroids in suspension (without embedding in agarose), while making selected localised
388 3D rheological measurements near them.
389
390 Extending the rheological measurements to 3D and sampling viscosity in 360 °, as shown in
391 our experiments with spheroids (Fig 6B), increases the capability of our measurements to
392 extract heterogeneities, not just between probe positions, but for different directions at a
393 single probe position. Currently, this 3D approach is restricted to computing viscosity in
394 liquids due to limited spatial sensitivity when tracking probe position in z (Methods). This is
395 not an issue when the extent of the Brownian motion of the probe is large, such as the ~1
396 µm (Fig 4B) observed in a weak optical trap in suspension culture, but is of concern when
397 motion is very small (≤ 50 nm) such as that observed in stiff gels (Fig 3B). In future the
398 sensitivity and measurement range of the 'sharpness' metric used for particle tracking in z
399 could be tuned by changing the plane spacing selected with the multiplane grating pair, the
400 probe size, the illumination levels and the signal to noise ratio of the images [24]. Efforts to
401 extend these 3D analyses to gels in the future would be highly valuable as biophysical
402 properties in the ECM are likely to vary in 3D, as apparent in the images of labelled collagen
403 present in the gel samples (Fig 5B).
404
405 The outputs from these proof-of-concept experiments are very data-rich. Different locations
406 of interest in the sample can be programmed to be revisited multiple times over a multi-day
407 experiment. As such, OptoRheo enables researchers to track numerous variables over time,
408 so that the relative cell and probe position, and cell behaviour (change in shape or size,
409 migration, apoptosis) can be related to viscous and elastic components of the matrix

biophysical properties. In future, it would be relatively straight forward to include additional probes into the sample (either genetically engineered reporters in the cells or sensors embedded in the gel/matrix) to track the coordinated impact of chemical, biological and mechanical cues.

As highlighted in recent publications [4,39], the control of cell behaviour by mechanical forces exerted through the ECM remains poorly understood, even as researchers take advantage of ECM control to create more complex, physiologically relevant models of development and disease, that better represent the *in vivo* micro-environment. The ability to integrate read-outs of cell behaviour with the microrheology of pericellular and distant matrix will be critical in further improving these models and using them to uncover the mechanistic basis of the phenomena they imitate. In addition, for development of therapeutics, there remains a significant gap in our understanding of the environments that drugs and delivery vehicles encounter in the body. The simultaneous observation of material transport together with rheological measurements will enable us to build detailed structure-function relations of drug delivery pathways, which in turn, will enable more efficient screening of candidate therapeutics and better predictive models of *in vivo* activity and efficacy.

Online Methods

Light sheet fluorescence microscopy (LSFM)

OptoRheo uses a reflected light sheet configuration where light sheet illumination is introduced into the imaging plane of an inverted microscope (Olympus IX-73) using a right-angle optic (90:10 RT beam splitter cube, 10 mm; Thorlabs Inc.). Z-scanning was achieved by moving the light sheet through the sample using a galvanometer scanning mirror (dynAXIS 3S; SCANLAB Gmbh) whilst simultaneously moving the

437 objective lens (LUMFLN60XW 60x 1.1 NA 1.5 mm WD; Olympus) via a
438 motorised piezo objective scanner (P-725.4CD; Physik Instrumente Ltd.) to keep the light
439 sheet in focus. Lateral positioning was achieved using a XY microscope stage (MS-2000,
440 ASI) and a zoom-mount attached to the cylindrical lens forming the light sheet. The
441 fluorescence image was detected using an sCMOS camera (Hamamatsu ORCA Flash 4.0
442 V2). Environmental control was achieved using an Okolab stage-top incubator (H301-K-
443 FRAME) supplied with pre-mixed CO_2 gas.

444

445 Multi-colour fluorescence imaging was made possible by using three lasers separately to
446 form the light sheet; 473 nm (SLIM-473; Oxxius), 532 nm (BWN-532-2OE; B&W Tek) and
447 640 nm (OBIS; Coherent). These laser lines were coupled to each other in the illumination
448 beam path using dichroic mirrors. A cylindrical lens (f = 50 mm, Thorlabs) was used to
449 generate the light sheet with a beam waist of 2.6 µm for λ_{ex} 473 nm, 2.4 µm for λ_{ex} 532 nm
450 and 3.3 µm for λ_{ex} 640 nm. The light sheet was aligned and characterised by imaging it in
451 reflection using two beam splitters (90:10 RT beam splitter cube, 5 mm; Thorlabs Inc.) in
452 tandem. The relationship between voltage applied to the galvanometer mirror and position of
453 the light sheet was characterised using this double beam splitter set up and keeping the
454 detection objective stationary while scanning the light sheet in z. The slope of the linear fit to
455 the measured position of the light sheet against the voltage applied gave the pixel to voltage
456 step size for synchronised movement.

457

458 When imaging samples, an autofocus step is first performed to ensure the illumination and
459 detection optics, primarily the objective, are aligned. This involves recording a stack of
460 images while keeping the imaging objective stationary and scanning the light sheet with a
461 sub-beam-waist step size. The frame with the highest mean intensity value denotes where
462 the light sheet waist coincides with the imaging plane and so the position of the light sheet
463 for this frame is synchronised with the height of the objective.

Standard off-the-shelf beam splitter cubes have a blunt edge that make the bottom 150 µm unsuitable for reflecting the light sheet illumination. These regions can be illuminated by tilting the light sheet at BS1 (Fig 1) or by using a bespoke cube with a sharp edge.

The mechanical components of the OptoRheo including the light sheet parts were controlled in LabVIEW (2018, 64bit; National Instruments Inc.). Image volumes were saved as '.tiff' files.

Image processing

Contrast adjustment and background subtraction was performed on image volumes in ImageJ/ Fiji [40] and volume tile stitching was performed using the BigStitcher [41] plugin for Fiji. 3D rendering for Figs 3C and 6A was done in FluoRender (v 2.26.3) [42].

To calculate the distance between microspheres and the nearest cell clusters, the centre positions of the microspheres in image coordinate space were extracted from the LSFM images. Although the microspheres (Polybead® Microspheres 6.00µm; PolySciences) were not fluorescently labelled, they are visible in the 3D LSFM images due to light scattering. Mesh renderings of the corresponding cell clusters were exported from FluoRender and these meshes along with positions of the microspheres from the same image volume were used as inputs in the point2trimesh.m [43] code in MATLAB which computes the shortest distance between a given point and the outer edge of a triangular mesh.

Figs 5A and 5B and the inset within 6A were prepared in MATLAB using mesh renderings generated in FluoRender overlaid with rendered spheres to depict the microsphere probes with a colour gradient to show the elastic modulus (G') (Fig 5A and 5B) or viscosity (Fig 6A inset) at each probe.

Optical Tweezers

The beam path from a continuous wave 1064 nm 5 W DPSS laser (Opus, Laser Quantum) was directed into the inverted microscope body and focused in the image plane using the same objective lens used for imaging in the LSFM set up. This objective lens was also used to image a small region of interest (14 μm x 14 μm) around the trapped polystyrene microspheres in wide-field with illumination in transmission for fast (300Hz) tracking of thermal fluctuations.

Multiplane detection

3D imaging of the micro-rheology probes was made possible by multiplane detection similar to the OpTIMuM instrument [24] and its predecessors [32,44]. Here, a multiplane grating pair was formed using two quadratically distorted diffraction gratings etched into a quartz substrate (bespoke production by Photronics UK Ltd). A single grating generates three sub-images, corresponding to the m = 0, ± 1 diffraction orders while two gratings with orthogonal etch patterns, can generate nine different sub-images, each corresponding to a different image depth which can be captured simultaneously on a single camera sensor (Hamamatsu ORCA Flash 4.0 V2) (Fig 4A). A 4f image relay system consisting of two 300 mm lenses was set up in the detection path between the camera and the inverted microscope body to enable the multiplane grating pair to be placed in the telecentric position. This set up ensured a consistent level of magnification in each of the imaging focal planes. The grating is on a slider and easily removable allowing the user to switch between standard full field of view imaging and multiplane imaging of a small region of interest with no adverse side effects. In our system we have used a relay and grating combination that gives plane separation of Δz = 0.79 μm with the nine images spanning 7.11 μm, designed to show the extent and position of our 6 μm diameter probe. Grating combinations can be chosen to suit the diameter of the

probe such that the total span in z covers the extent of the trajectory of the probe with the minimum plane separation for optimal resolution [24].

Microrheology

Particle tracking microrheology was performed using polystyrene microspheres as probes (Polybead® Microspheres 6.00µm diameter; PolySciences). In hydrogel cultures, the microspheres were encapsulated during the gelation process at a final dilution of 1:200,000 v/v from concentrate product. In suspension cultures, the microspheres were added to a final dilution of 1:200,000 from concentrate product, the probes were individually optically trapped using ~4 mW of laser power (at the sample) and moved to a position of interest. The Brownian motion displayed by the microspheres, was recorded over 300,000 frames at ~300 frames per second using OptoRheo with illumination in transmission from an LED light source (Fig 1). Videos of the microsphere probes were acquired using Micro-Manager (version 1.4) [45].

The time-dependent trajectories of the microspheres were extracted from these videos in MATLAB (2019b; MathWorks, Nattick, MA). For 2D trajectories along the image plane a centre-of-mass detection method following Otsu's method of multiple thresholding (with two levels) was used. Out-of-plane Z motion of the probe was tracked by computing a 'Sharpness' metric as detailed in our OpTIMuM publication [24]. Particle tracking with these methods gives us a minimum sensitivity of ~ 15 nm (FWHM) in the xy plane and ~ 30 nm (FWHM) in z for a particle with diameter of ~ 6 µm, using a 60x objective and a plane spacing of ~ Δz = 0.79 µm [24]. A calibration step is performed for each microsphere before taking a measurement by translating a lens (L4 in Fig 1) in the beam expander in the optical path as described previously [24].

In the case of hydrogels, the Brownian motion of the microsphere confined within the gel was recorded in 2D without the use of the optical trap or multiplane imaging. For these data, an analysis of the mean squared displacement (MSD) gave the storage (elastic) and loss (viscous) moduli of the gel. To acquire direction-averaged viscoelastic measurements for each probe, first the experimentally acquired trajectory along the x axis was detrended to remove long-term drift and was subjected to a rotational transformation around the y axis at 20º intervals from 0° to 180°, to resample the trajectory along different directions. The MSD values for each resampled trajectory was then calculated and these MSD curves were fit to equation 1, a simple model for a Maxwell material characterised by a single relaxation time, which accounts for the solid-like nature of the hydrogels and the pseudo diffusive behaviour of the probe particle [46].

$$MSD(t) = A + B\left(1 - \exp\left(-\frac{t}{\tau}\right)\right) \quad (1)$$

A, B and τ are fitting parameters. This approach mitigates any error generated by the inherently finite nature of the measurements that affects the accuracy to which the MSD is calculated especially at such short-time scales (Fig 3). The MSD relates to the gel's time dependent compliance J(t) [47] as follows,

$$MSD(t) = \frac{k_B T}{\pi a} J(t) \quad (2)$$

where k_B is the Boltzmann's constant, T is the absolute temperature, and a is the radius of the microsphere. The materials' complex shear modulus can be computed from the materials' compliance by means of its Fourier transform ($\hat{J}(\omega)$)

$$G^*(\omega) = \frac{1}{i\omega\hat{J}(\omega)} . \quad (3)$$

We used a new MATLAB based graphical user interface named π-Rheo (see code availability statement) for evaluating Equations 2 & 3, to compute the Fourier transform of the particles' MSD and the materials' complex modulus for passive microrheology measurements. π-Rheo is underpinned by the algorithm introduced in i-RheoFT [48]. The real

and imaginary parts of the complex modulus give the elastic (G') and viscous (G'') moduli of the gel. Values reported are mean values over the explored frequency range.

For aqueous solutions, where 3D positions of the probe are tracked, the viscosity may be extracted by fitting an exponential decay against the normalised position autocorrelation function [34]. This method is highly effective for data aligned with the principal axes of the optical trap (see Fig 4D). However, when calculating viscosity along vectors not aligned with these axes using this method, the significant trap anisotropy along the z-axis introduces artefacts as outlined in detail previously [49]. Alternatively, if the material under investigation is purely viscous, then at very early times the MSD of the bead should behave as if the bead is not trapped. Under these conditions, Fick's Law for unconstrained diffusion can be used to extract viscosity in any arbitrary direction rather than just x, y, z at these early times. Fick's law for motion in 1D is given by,

$$MSD_{(t,\theta,\varphi)} = 2D_{(\theta,\varphi)}t \tag{4}$$

where θ and ψ define the direction being probed and D is the diffusion coefficient for a sphere of radius a in a liquid with viscosity η. From the Stokes-Einstein relation

$$D = \frac{k_B T}{6\pi\eta_{(\theta,\varphi)}a}\,. \tag{5}$$

This approach was used to compute viscosity in 3D as shown in Fig 4E and Fig 6A.

Cell culture

The breast cancer cell line MCF7 expressing tdTomato was maintained in high glucose DMEM (Life Technologies; 21969-035) with 10 % foetal bovine serum (Life Technologies, 10500-064), 1 % L-glutamine (Life Technologies, 25030-024). To maintain the tdTomato protein expression, the medium was supplemented with Puromycin 1:1000 (Gibco, A11138-03) at every passage. Cells were maintained at 37 °C and 5 % CO_2 in a humidified atmosphere during cell culture and measurements on the OptoRheo.

Peptide gel precursor preparation

The precursor and gel preparation method was followed as previously published [50]. A commercially available peptide preparation in powder form was used as the source of the octapeptide gelator (Pepceuticals UK, FEFEFKFK, Phe-Glu-Phe-Glu-Phe-Lys-Phe-Lys). To form the precursor, a mass of 10 mg peptide preparation was dissolved in 800 µL sterile water (Sigma, W3500), using a 3 min vortex step followed by centrifugation (3 min at 1000 rpm) and a 2 hour incubation at 80 °C. After incubation, 0.5 M NaOH (Sigma, S2770) was added incrementally to the gel until optically clear. The gel was vortexed, buffered by addition of 100 µL 10× PBS (Gibco, 70011), and incubated at 80 °C overnight. The resulting precursor could be stored at 4 °C until required.

Peptide gel formation with collagen I supplementation

Prior to peptide gel formation, the precursor was heated at 80 °C until liquid to ensure homogeneity, before transferring to a 37 °C water bath. Cy5 labelled (in-house preparation, see method below) rat tail Collagen I was neutralised directly before use with 1M NaOH according to manufacturer instructions, and diluted with sterile water and 10x PBS to a concentration of 1 mg/mL while keeping on ice at all times to prevent polymerisation. Peptide gel formation was then induced by pH neutralisation on addition of cell culture medium (with or without cell suspension) to the gel precursor. A final volume of 1.25 mL was obtained from a preparation by adding 125 µL of cell suspension and 125 µL Cy5 collagen I to a precursor volume of 1 mL. The end concentration of peptide preparation was 8 mg/mL and collagen I concentration was 100 µg/mL. Polystyrene microspheres (Polybead® Microspheres 6.00µm; PolySciences) were added at final density of approx. $3x10^5$/mL. The medium / cell suspension was thoroughly mixed with the precursor and Collagen-I by gentle (reverse) pipetting, before plating at 100 µL per well into a 4 µ-well glass bottom chambered coverslips

(IBIDI, 80427) pre-mounted with a beamspliter cube (ThorLabs, BS070). The wells were then flooded with cell culture medium and incubated at 37 °C and 5 % CO_2 in a humidified atmosphere. Sequential media changes (at least two) over the next 2 hours ensured complete neutralisation and therefore gelation.

For cell encapsulation, the 125 µL volume of cell culture medium was prepared as a cell suspension at 1.25 x the intended final seeding density, to allow for the dilution factor on mixing with the gel precursor. Trypsin-EDTA (0.25%; Life Technologies, 25200056) was used to detach cells from 2D culture at sub-confluence. Cells were re-suspended in 125 µL cell culture medium at a density of 1.25×10^5 cells/mL, giving final seeding density in the peptide gel 1x 10^5 cells/mL. 24 hrs post encapsulation culture medium was replenished, with the addition of HEPES buffer (Life Technologies, 15630-056) at 10 mM final concentration.

Prior to casting the gel, the beam splitter cubes were sterilised in absolute ethanol. Cubes were soaked for 1hour, then left to dry on a paper tissue inside the class 2 safety cabinet. To minimise movement and consequently damage to delicate structure of a hydrogel, the cubes were secured in place with glass coverslips.

Collagen gel labelling with Cy5

Rat tail collagen type 1 gel (10 mL; Gibco, A1048301) was dissolved in 0.1 M sodium bicarbonate buffer (10 mL, pH 8.5) and 110 µL Cy5 NHS ester solution (10 mg/mL, DMSO) added. The reaction mixture was stirred at 4 °C overnight. The reaction mixture was purified via the dialysis method at 4 °C to remove the unreacted dye and yield the Cy5 labelled collagen. It was then lyophilised and reconstituted in 20 mM acetic acid buffer.

Spheroid preparation

Corning 7007 Ultra-low attachment (ULA) 96-well round-bottom plates were used to culture the 3D spheroids. 80 % confluent tdTomato MCF-7 monolayer cells were detached, collected and the cell number determined using an automated cell counter (Biorad TC20). A single-cell suspension was diluted in culture medium and cells seeded at 6000 cells/well to generate the spheroids (final volume of cell suspension in each well was 100 µL). The plates were then centrifuged at 300 RCF for 5 min and cultured for 3 days until visible spheroid formation.

For experiments on the OptoRheo, spheroids were placed in 4 µ-well glass bottom chambered coverslips (IBIDI, 80427) using a P1000 pipette with the pipette tip cut off at the end. Each spheroid was placed singularly in 500 µL of phenol-free nutrient media (1:1 DMEM:F12 supplemented with 10% FBS) per well and ~ 5 mm away from the edge of a 10 mm beam splitter cube (ThorLabs, BS070) (Fig S1 A) to enable LSFM imaging. Similar to the peptide gel sample preparation protocol, beam splitter cubes were sterilised between uses and secured in place in the chambered coverslips by wedging glass coverslips between the cube and the chamber side wall.

Data Availability

Data will be made available at the time of peer-reviewed publication.

Code Availability

π-Rheo software will be available to download as a supplementary information file (Supplementary software) at the time of peer-reviewed publication.

References

1. Discher, D. E., Janmey, P. & Wang, Y. Tissue Cells Feel and Respond to the Stiffness of Their Substrate. *Science* **310**, 1139–1143 (2005).
2. Lo, C. M., Wang, H. B., Dembo, M. & Wang, Y. L. Cell movement is guided by the rigidity of the substrate. *Biophys. J.* **79**, 144–152 (2000).
3. Pelham, R. J. & Wang, Y. Cell locomotion and focal adhesions are regulated by substrate flexibility. *Proc. Natl. Acad. Sci.* **94**, 13661–13665 (1997).
4. Veenvliet, J. V., Lenne, P.-F., Turner, D. A., Nachman, I. & Trivedi, V. Sculpting with stem cells: how models of embryo development take shape. *Development* **148**, dev192914 (2021).
5. Fernandez, P. & Bausch, A. R. The compaction of gels by cells: a case of collective mechanical activity. *Integr. Biol.* **1**, 252–259 (2009).
6. Bloom, R. J., George, J. P., Celedon, A., Sun, S. X. & Wirtz, D. Mapping Local Matrix Remodeling Induced by a Migrating Tumor Cell Using Three-Dimensional Multiple-Particle Tracking. *Biophys. J.* **95**, 4077–4088 (2008).
7. Lu, P., Weaver, V. M. & Werb, Z. The extracellular matrix: A dynamic niche in cancer progression. *J. Cell Biol.* **196**, 395–406 (2012).
8. Long, Y., Niu, Y., Liang, K. & Du, Y. Mechanical communication in fibrosis progression. *Trends Cell Biol.* **32**, 70–90 (2022).
9. Meng, H. & Nel, A. E. Use of Nano Engineered Approaches to Overcome the Stromal Barrier in Pancreatic Cancer. *Adv. Drug Deliv. Rev.* **130**, 50–57 (2018).
10. Piersma, B., Hayward, M. K. & Weaver, V. M. Fibrosis and cancer: A strained relationship. *Biochim. Biophys. Acta Rev. Cancer* **1873**, 188356 (2020).
11. Ashworth, J. C. *et al.* Peptide gels of fully-defined composition and mechanics for probing cell-cell and cell-matrix interactions in vitro. *Matrix Biol.* (2019) doi:10.1016/j.matbio.2019.06.009.

12. Chaudhuri, O. Viscoelastic hydrogels for 3D cell culture. *Biomater. Sci.* **5**, 1480–1490 (2017).
13. Chaudhuri, O., Cooper-White, J., Janmey, P. A., Mooney, D. J. & Shenoy, V. B. Effects of extracellular matrix viscoelasticity on cellular behaviour. *Nature* **584**, 535–546 (2020).
14. Charrier, E. E., Pogoda, K., Wells, R. G. & Janmey, P. A. Control of cell morphology and differentiation by substrates with independently tunable elasticity and viscous dissipation. *Nat. Commun.* **9**, 449 (2018).
15. Greiss, F., Deligiannaki, M., Jung, C., Gaul, U. & Braun, D. Single-Molecule Imaging in Living Drosophila Embryos with Reflected Light-Sheet Microscopy. *Biophys. J.* **110**, 939–946 (2016).
16. Beicker, K., O'Brien, E. T., Falvo, M. R. & Superfine, R. Vertical Light Sheet Enhanced Side-View Imaging for AFM Cell Mechanics Studies. *Sci. Rep.* **8**, 1504 (2018).
17. Kashekodi, A. B., Meinert, T., Michiels, R. & Rohrbach, A. Miniature scanning light-sheet illumination implemented in a conventional microscope. *Biomed. Opt. Express* **9**, 4263 (2018).
18. Gustavsson, A. K., Petrov, P. N., Lee, M. Y., Shechtman, Y. & Moerner, W. E. 3D single-molecule super-resolution microscopy with a tilted light sheet. *Nat. Commun.* **9**, (2018).
19. Buchmann, B. *et al.* Mechanical plasticity of collagen directs branch elongation in human mammary gland organoids. *Nat. Commun.* **12**, 2759 (2021).
20. Hafner, J. *et al.* Monitoring matrix remodeling in the cellular microenvironment using microrheology for complex cellular systems. *Acta Biomater.* **111**, 254–266 (2020).
21. Ciccone, G. *et al.* What Caging Force Cells Feel in 3D Hydrogels: A Rheological Perspective. *Adv. Healthc. Mater.* 2000517 (2020) doi:10.1002/adhm.202000517.
22. Han, Y. L. *et al.* Cell swelling, softening and invasion in a three-dimensional breast cancer model. *Nat. Phys.* **16**, 101–108 (2020).
23. Guadayol, Ò. *et al.* Microrheology reveals microscale viscosity gradients in planktonic systems. *Proc. Natl. Acad. Sci.* **118**, (2021).

24. Matheson, A. B. *et al.* Optical Tweezers with Integrated Multiplane Microscopy (OpTIMuM): a new tool for 3D microrheology. *Sci. Rep.* **11**, 5614 (2021).
25. Huisken, J., Swoger, J., Del Bene, F., Wittbrodt, J. & Stelzer, E. H. K. Optical Sectioning Deep Inside Live Embryos by Selective Plane Illumination Microscopy. *Science* **305**, 1007–1009 (2004).
26. Pitrone, P. G. *et al.* OpenSPIM: an open-access light-sheet microscopy platform. *Nat. Methods* **10**, 598–599 (2013).
27. Reynaud, E. G., Krzic, U., Greger, K. & Stelzer, E. H. K. Light sheet-based fluorescence microscopy: more dimensions, more photons, and less photodamage. *HFSP J.* **2**, 266–75 (2008).
28. Hu, Y. S. *et al.* Light-sheet Bayesian microscopy enables deep-cell super-resolution imaging of heterochromatin in live human embryonic stem cells. *Opt. Nanoscopy* **2**, 7 (2013).
29. Gebhardt, J. C. M. *et al.* Single-molecule imaging of transcription factor binding to DNA in live mammalian cells. *Nat. Methods* **10**, 421–426 (2013).
30. Tassieri, M. Microrheology with optical tweezers: peaks & troughs. *Curr. Opin. Colloid Interface Sci.* **43**, 39–51 (2019).
31. Lee, M. P., Padgett, M. J., Phillips, D., Gibson, G. M. & Tassieri, M. Dynamic stereo microscopy for studying particle sedimentation. *Opt. Express* **22**, 4671 (2014).
32. Blanchard, P. M. & Greenaway, A. H. Simultaneous multiplane imaging with a distorted diffraction grating. *Appl. Opt.* **38**, 6692 (1999).
33. Dasgupta, R., Verma, R. S., Ahlawat, S., Chaturvedi, D. & Gupta, P. K. Long-distance axial trapping with Laguerre–Gaussian beams. *Appl. Opt.* **50**, 1469–1476 (2011).
34. Tassieri, M. *et al.* Microrheology with Optical Tweezers: Measuring the relative viscosity of solutions 'at a glance'. *Sci. Rep.* **5**, 8831 (2015).
35. Pal, A. *et al.* A 3D Heterotypic Breast Cancer Model Demonstrates a Role for Mesenchymal Stem Cells in Driving a Proliferative and Invasive Phenotype. *Cancers* **12**, 2290 (2020).

751 36. Vasudevan, J., Lim, C. T. & Fernandez, J. G. Cell Migration and Breast Cancer
752 Metastasis in Biomimetic Extracellular Matrices with Independently Tunable Stiffness.
753 *Adv. Funct. Mater.* **30**, 2005383 (2020).
754 37. Lovitt, C. J., Shelper, T. B. & Avery, V. M. Doxorubicin resistance in breast cancer cells
755 is mediated by extracellular matrix proteins. *BMC Cancer* **18**, 41 (2018).
756 38. Leach, J. *et al.* Comparison of Faxén's correction for a microsphere translating or
757 rotating near a surface. *Phys. Rev. E* **79**, 026301 (2009).
758 39. Gjorevski N. *et al.* Tissue geometry drives deterministic organoid patterning. *Science*
759 **375**, eaaw9021 (2022).
760 40. Schindelin, J. *et al.* Fiji: an open-source platform for biological-image analysis. *Nat.*
761 *Methods* **9**, 676–82 (2012).
762 41. Hörl, D. *et al.* BigStitcher: reconstructing high-resolution image datasets of cleared and
763 expanded samples. *Nat. Methods* **16**, 870–874 (2019).
764 42. Wan, Y. *et al.* FluoRender: joint freehand segmentation and visualization for many-
765 channel fluorescence data analysis. *BMC Bioinformatics* **18**, 280 (2017).
766 43. Frisch, D. Point2trimesh () distance between point and triangulated surface. *MATLAB*
767 *Cent. File Exch.* **25**, (2016).
768 44. Dalgarno, P. A. *et al.* Multiplane imaging and three dimensional nanoscale particle
769 tracking in biological microscopy. *Opt. Express* **18**, 877 (2010).
770 45. Edelstein, A., Amodaj, N., Hoover, K., Vale, R. & Stuurman, N. Computer Control of
771 Microscopes Using μManager. *Curr. Protoc. Mol. Biol.* **92**, 14.20.1-14.20.17 (2010).
772 46. Alshareedah, I., Moosa, M. M., Pham, M., Potoyan, D. A. & Banerjee, P. R.
773 Programmable viscoelasticity in protein-RNA condensates with disordered sticker-
774 spacer polypeptides. *Nat. Commun.* **12**, 6620 (2021).
775 47. Tassieri, M., Evans, R. M. L., Warren, R. L., Bailey, N. J. & Cooper, J. M. Microrheology
776 with optical tweezers: Data analysis. *New J. Phys.* **14**, 115032 (2012).
777 48. Smith, M. G., Gibson, G. M. & Tassieri, M. i-RheoFT: Fourier transforming sampled
778 functions without artefacts. *Sci. Rep.* **11**, 24047 (2021).

49. Matheson, A. B. *et al.* Microrheology With an Anisotropic Optical Trap. *Front Phys* **9**, 621512 (2021).

50. Ashworth, J. C. *et al.* Preparation of a User-Defined Peptide Gel for Controlled 3D Culture Models of Cancer and Disease. *J. Vis. Exp. JoVE* (2020) doi:10.3791/61710.

Acknowledgements

The authors acknowledge support via linked EPSRC grants EP/R035067/1, EP/R035563/1, and EP/R035156/1 and NC3Rs grants NC/T001259/1 and NC/T001267/1.

The MCF-7 tdTomato cell line was provided by and with thanks to Prof. Anna Grabowska, University of Nottingham.

Competing Interests

The authors declare no conflicts of interest.

Supplementary Information

1. Sample preparation

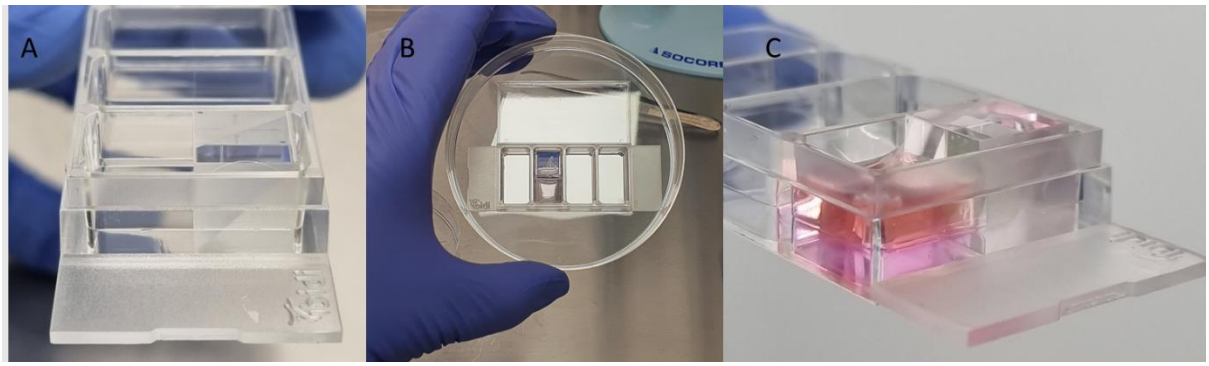

Fig S1: Sample set up: A. Side view of the 4 µ-well chambered coverslip with a 10 mm beam splitter cube inserted with the reflective surface facing the empty half of the chamber. B. Top view of a sample with the gel cast next to the beam splitter cube. C. Side view of the peptide hydrogel topped up with medium next to the beam splitter cube.

805 2. Supplementary table: Viscoelasticity values per gel condition and day

	Condition	G' (mean) [Pa]	G' (var) [Pa]	G'' (mean) [Pa]	G'' (var) [Pa]
Day 1	gel	9.38	3.82	1.75	0.43
	gel + cells	10.09	7.64	1.73	0.06
	gel + collagen	7.68	13.42	1.31	0.25
	gel + collagen + cells	10.06	6.19	1.71	0.18
Day 2	gel	7.79	9.90	1.14	0.17
	gel + cells	8.74	7.69	1.32	0.20
	gel + collagen	7.34	9.05	1.27	0.15
	gel + collagen + cells	8.68	24.19	1.56	1.84
Day 3	gel	5.88	5.20	0.96	0.15
	gel + cells	7.71	7.44	1.24	0.15
	gel + collagen	6.73	5.34	1.02	0.11
	gel + collagen + cells	7.83	43.97	1.82	4.95

806

807 Table S1: Mean and variance of G' and G'' measurement values for different gel conditions

808 over three days.

809

810

811 3. Spatiotemporal changes in viscoelastic measurements

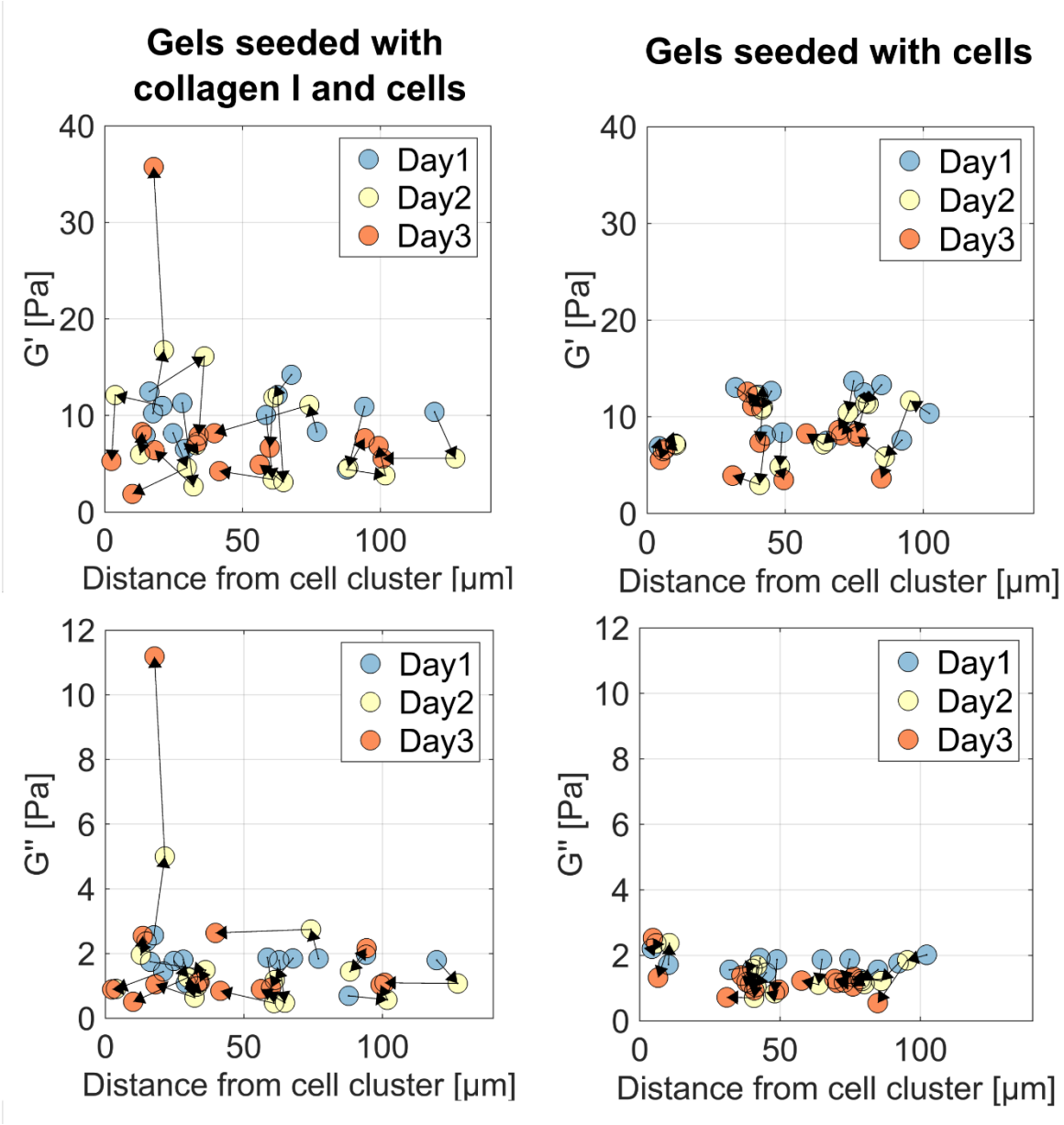

812

813 Fig S2: Changing elastic (G') and viscous (G'') moduli values with changing relative distance

814 between probes and cell clusters in gel with (left top and bottom) and without (right top and

815 bottom) collagen over three days.